Advanced Steel Construction – Vol. 19 No. 3 (2023) 242–253
DOI:10.18057/IJASC.2023.19.3.5

NONLINEAR FINITE ELEMENT ANALYSIS OF ALL-STEEL BUCKLING RESTRAINED BRACES

Prachi Mishra [1, *] and Arvind Y. Vyavahare [2]

[1] *PhD Scholar, Visvesvaraya National Institute of Technology, Nagpur 440022, India*
[2] *Associate Professor, Visvesvaraya National Institute of Technology, Nagpur 440022, India*
** (Corresponding author: E-mail: dt19amc001@students.vnit.ac.in)*

ABSTRACT

Buckling restrained braces are gaining popularity in earthquake-resistant designs these days. These braces give stable hysteretic behaviour with a non-buckling steel core encased in a steel tube, that is filled with concrete or mortar. However, in the last few years, researchers have observed that these braces do not need any filler material and can be all-steel. This study aims to carry out a parametric study on All-Steel Buckling Restrained Braces (ASBRBs) by varying the restraining mechanism, the amount of gap between the core and the restrainer, and loading protocols. This paper presents a parametric study conducted on 12 proposed ASBRBs through non-linear finite element analysis. The proposed models have identical inner steel core cross-sections, but the restraining mechanism differs in each case. This paper also includes an experimental study on two small-scale ASBRB specimens. In addition, a finite element study on the effect of variation in stiffness of the transition portion of the core on different performance parameters is carried out. The parameters investigated include hysteretic response, energy dissipation, compression adjustment factor, and strain hardening adjustment factor. The results indicated that the global buckling behaviour of ASBRBs is significantly influenced by the restraining mechanism. In addition, this study also revealed that the global buckling behaviour does not significantly depend on the spacing of the restrainers. It was also observed that BRBs with unstiffened cores show stable hysteretic behaviour up to 2% strain, which deteriorates with further increase in the strain.

ARTICLE HISTORY

Received: 6 September 2022
Revised: 24 April 2023
Accepted: 10 May 2023

KEYWORDS

ASBRB;
Hysteretic behavior;
Restraining mechanism;
FE analysis;
Steel

1. Introduction

Buckling Restrained Braces (BRBs) represent a cutting-edge seismic device widely utilized in contemporary construction practices for steel and reinforced concrete (RC) buildings located in earthquake-prone regions. These innovative devices serve as effective energy dissipators, surpassing the seismic performance achieved by conventional bracing systems. Unlike conventional braces, which demonstrate unstable hysteretic behavior and fail to dissipate energy under compression, BRBs leverage a robust restraining mechanism that induces buckling prior to yielding, allowing for substantial energy dissipation during seismic events. Fig. 1 illustrates the contrasting hysteretic behavior between a BRB and a conventional brace. BRBs exhibit improved performance in both tension and compression, making them a noteworthy modification to conventional bracing systems. The fundamental concept revolves around restraining brace buckling by employing a metal core encapsulated within a buckling restraining mechanism, effectively preventing core buckling. This restraining mechanism consists of a steel outer cover enveloping the steel core, which is subsequently filled with a filler material such as mortar or plain concrete. The filler plays an important role in the energy dissipating behavior of BRBs [1]. Furthermore, the core is coated with a non-adhesive substance to prevent the restrainer from adhering to the inner metal core, thereby averting the transfer of axial load from the restrainer to the core. In contemporary practice, All-Steel Buckling Restrained Braces (ASBRBs) have gained preference over conventional filler BRBs due to their advantageous characteristics, including reduced weight, simplified installation, handling, and maintenance. Moreover, ASBRBs can be disassembled and inspected following seismic events, facilitating replacement if necessary. Fig. 2 presents a visual representation of a typical all-steel BRB concept.

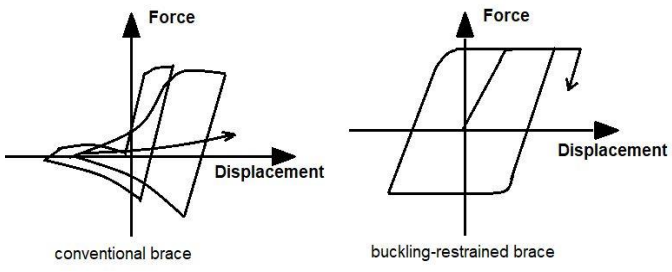

Fig. 1 Hysteretic behavior of a conventional brace and a BRB

The concept of BRBs originated in Japan, with Wakabayashi et al. [2] being the pioneers who conducted experiments on panel BRBs. Subsequently, Kano et al. [3] conducted a numerical study on the elastoplastic behavior of BRBs, while Kimura et al. [4] proposed the idea of fabricating BRBs to address the degradation of bearing capacity and stiffness. These proposed BRBs also addressed the requirements of reducing ductility and enhancing energy dissipation capacity in ordinary steel braces under compression. Mochizuki et al. [5, 6] conducted research to tackle the overall stability issues of steel braces surrounded by reinforced concrete.

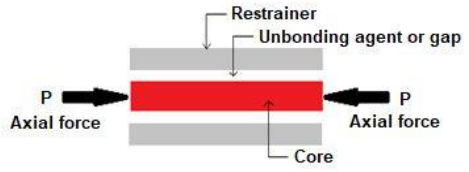

Fig. 2 Concept of all-steel BRB

Despite the positive responses and numerous research conducted on BRBs, they were not included in the design recommendations of the Architectural Institute of Japan (AIJ) until 1996. Fujimoto et al. [7] carried out research on BRBs with steel cores encased in steel tubes filled with concrete or mortar. In 1989, these BRBs were first practically applied in two steel-framed office buildings [8], and since then, they have been employed in approximately 160 buildings in Japan [9]. By 1990, more than a hundred buildings in Japan had adopted and utilized BRBs, with the majority of them being taller than 15 stories. Additionally, Wada et al. [10] introduced a new concept called "damage tolerant" design, where BRBs were utilized as energy dissipating elastoplastic dampers within an elastic mainframe. The acceptance and implementation of BRBs in Japan significantly increased, particularly after the 1995 Kobe earthquake.

After demonstrating successful performance in Japan, the technology of BRBs was transferred to the United States (US). A significant turning point in seismic research for steel structures in the US was the Northridge earthquake in 1994. Prior to this event, it was widely believed that special moment-resisting frames were effective solutions for earthquake-resistant design. However, the brittle failure of beam-to-column moment connections in numerous multi-story steel buildings during the earthquake compelled researchers to reassess and revise the seismic design provisions.

The first practical application of BRBs in the US occurred in 1998 with the construction of a building at the University of California (UC) Davis, followed

by testing at UC Berkeley in 2000. Subsequently, several projects utilizing BRBs were executed within a span of a few years. Black et al. [11] conducted component testing on the braces and observed repeating symmetrical hysteretic behavior. The seismic behavior of these braces was extensively investigated by Sabelli et al. [12]. Consequently, with the inclusion of design guidelines for BRB frames in the Seismic Provisions for Structural Steel Buildings [13], numerous buildings incorporating BRBs were constructed across the US. Fahenstock et al. [14] conducted large-scale pseudo-dynamic numerical analyses on the braces, further enhancing understanding of their behavior. The design standards for these braces are provided by AISC 341-10 [15], which establishes the guidelines for their implementation.

Numerous numerical models have been developed to accurately simulate the behavior of BRBs. In the present study, a comprehensive parametric analysis was conducted on 12 ASBRBs. Each ASBRB is characterized by a distinct restraining mechanism, varying gap sizes between the core and the restrainer, different core configurations (stiffened and unstiffened), and diverse loading protocols. The primary objective is to examine the influence of these parameters on the hysteretic behavior of all-steel BRBs. The study aims to identify the most cost-effective ASBRB configuration that maximizes energy dissipation under different loading conditions. By assessing these factors, valuable insights can be gained into optimizing the performance of ASBRBs in structural applications.

2. Basic concept

2.1. Concept

BRB is based on a very simple concept that is to restrict buckling and thereby show symmetrical and stable hysteretic behavior. This improves the energy absorption capability of the brace. A BRB is made up of the following components:

I. A metallic core placed centrally to yield,
II. A buckling-restraining mechanism to encase the core and restrain its global buckling, and
III. An un-bonding agent between the encasing restraint and the core so as to allow for the free expansion of the core element under cyclic loading and also to restrict the adhering of the core and the restraint.

2.2. Stability analysis

There are three major buckling modes under which BRB is to be identified [11].

1. Global buckling of the brace under axial compression.
2. Local buckling of the metallic core
3. Torsional buckling of the portion of the extended part of the core

The global stability of the brace can be found directly from Euler's theory of buckling which states that the critical load of the brace, P_{cr} is simply the Euler buckling load of the outer tube, P_e. Hence, when the Euler buckling load of the tube, P_e is greater than the yielding load of the inner metallic core, P_y, the brace is ensured in its global stability. Here,

$$P_e = \frac{\pi^2 EI_{tube}}{KL^2} \tag{1}$$

$$P_y = \sigma_y A_{core} \tag{2}$$

Where, EI_{tube} is the flexural rigidity of the outer tube, KL is the effective length of the entire brace, σ_y is the yield stress of the inner metallic core, and A_{core} is the cross-section area of the core.

Hence, for the global stability criteria, the ratio of the Euler load of the tube to the yield load of the core should be greater than 1. i.e.

$$\frac{P_e}{P_y} > 1 \tag{3}$$

For the local buckling mode, Wada et al. [10] came up with an equation for the critical load for the local buckling of the inner core as

$$P_{cr} = 2\sqrt{\beta E_i I_i} \tag{4}$$

Where, E_iI_i is the flexural rigidity for the inner steel core and β is the distributed spring constant.

It was observed that the efficiency of the brace can be enhanced when the buckling of the inner core along the restrained length does not take place.

High order buckling of the inner steel core can be avoided when,

$$P_{cr} \geq \sigma_y A_i \tag{5}$$

Which requires,

$$\beta \geq \frac{\sigma_y^2 A_i^2}{4E_i I_i} \tag{6}$$

Where, A_i is the cross-section area of the inner core. It was also observed that in higher modes, the critical load of the inner steel core does not depend upon the end conditions of the core [16].

The portion of the core that extends from the casing may undergo torsional buckling, which is the third and most critical mode of buckling for BRB. Many research [17, 18, 19] have been made, and some are still in progress, on the torsional buckling behavior of BRBs. Researchers have proven that the critical load causing torsional buckling of the extruded part in BRB does not depend upon the length of the extension [11]. However, the seismic performance of the brace depends on the length of the connectors [20].

3. Experimental study

3.1. Description of specimens fabricated

In order to study the actual behavior of ASBRBs, two small scale specimens of proposed ASBRBs are prepared and tested experimentally. The ASBRB specimens fabricated are similar to the proposed BRB models used for parametric study in the latter section. The core part of specimen 1 is made up of a rectangular steel plate of 15 mm x 3 mm size, and specimen 2 is of 18 mm x 3 mm plate size. Both plates have a yield strength of 250 MPa. The specimens are restrained with bolted connections. Both specimens have a different core cross-section but an identical restraining arrangement. The overall length of the specimens is 500 mm, with a yielding core length of 400 mm. The detailed dimensions and properties of both specimens tested are given in Table 1. Detailing of both ASBRBs is shown in Fig. 3.

Table 1
Properties of parts of specimens fabricated

Specimen	Parts	Dimension	Elastic Modulus (GPa)	Density (kg/m^3)
1.	Core plate	15 mm x 3 mm	210	7780
	Restrainer	Four ISA 35x35x5	210	7760
	Filler plates	10 mm x 3 mm	210	7760
2.	Core plate	18 mm x 3 mm	210	7780
	Restrainer	Four ISA 35x35x5	210	7760
	Filler plates	10 mm x 3 mm	210	7760

Four angle sections are used for restraining the core plate for both specimen 1 and specimen 2. Two filler plates are provided along the length of the core plates to facilitate bolting of the restrainer angle sections. A gap of 2 mm is kept between the filler plates and the core plate. A 1 mm thick sheet of polyflurotetraehtylene (PTFE) is coated on the core plate to avoid friction between the angle restrainers and the core part. The restrainers are connected to each other by bolted connections. 6 mm diameter bolts are provided at a centre-to-centre spacing of 40 mm.

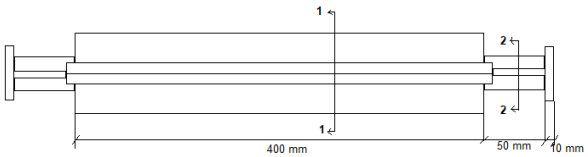

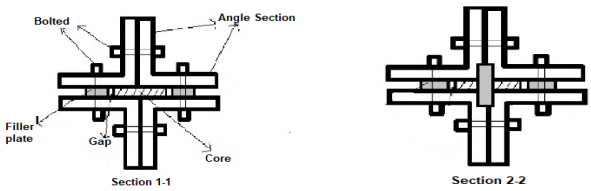

Fig. 3 Cross-sectional details of specimens

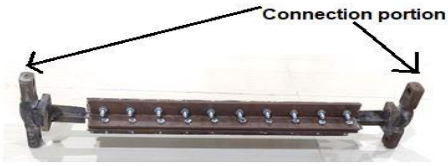

Fig. 4 Specimen 1

3.2. Loading protocol and experimental setup

The loading protocol for both specimens is according to the AISC provisions [13], i.e. $\pm\Delta_y$, $\pm 0.5\Delta_{bm}$, $\pm\Delta_{bm}$, $1.5\pm\Delta_{bm}$ and $\pm 2.0\Delta_{bm}$, but the number of cycles in each level is being increased to get more accurate results. The yield displacement, Δ_y for both specimens is found out to be 0.5 mm, and the ultimate displacement, Δ_{bm} is assumed to be 1% axial strain, which is 4 mm. Fig. 5 depicts the loading pattern, which consists of 5 sets of displacement levels with each level having 4 cycles. The specimens are tested in a shock absorber testing machine, and cyclic loading is given in five steps with four cycles each.

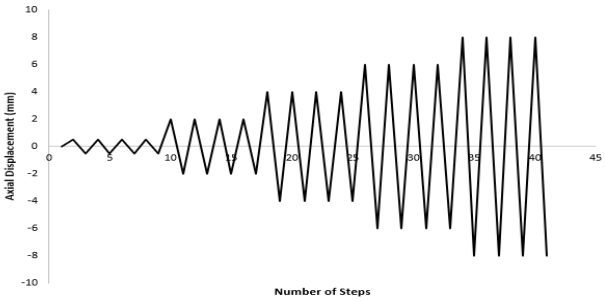

Fig. 5 Loading protocol

Both specimens are welded to end plates of size 50 mm x 35 mm x 10 mm on either end of the core plate. Further, the end plates are welded to the connection portion to enable the specimens to be installed in the testing machine. Fig. 4 shows the fabricated view of specimen 1. The specimens are fixed to the testing machine with the respective connecting parts. Fig. 6 shows the test setup for both specimens. The upper end of the specimen is kept fixed while the displacement cycles are applied through the lower part. Required inputs are given to the testing machine, and a force versus displacement plot is received as an output. A test frequency of 0.5 hertz is given for each displacement level as obtained from the loading protocol. Testing strokes are given as ±0.5 mm, ±2 mm, ±4 mm, ± 6 mm and ±8 mm for respective five displacement levels.

3.3. Experimental results

The hysteretic behavior of the two specimens tested can be plotted with force-displacement values received as an output from the shock absorber machine. It was observed that both showed symmetrical hysteretic behavior with optimum energy dissipation (Fig. 7). It is observed from the hysteretic behavior of both specimens that specimen 2 dissipated more energy than specimen 1. The failure pattern observed in the core parts of both specimens is shown in Fig. 8.

Specimen 1

No global buckling was observed in specimen 1, as expected, since the restrainer provided was as per Euler's global buckling criteria (explained in 2.2). Local buckling was observed along the yielding length of the core. The specimen dissipated a considerable amount of energy, but shear failure occurred at the transition portion on reaching 2% axial strain loading.

Specimen 2

Specimen 2 showed local buckling along with a little lateral bucklng about the weaker plane. A desirable amount of energy dissipation was observed with no global buckling, and hence it can be considered that the specimen can be further loaded after 2% axial strain.

Fig. 6 Test setup

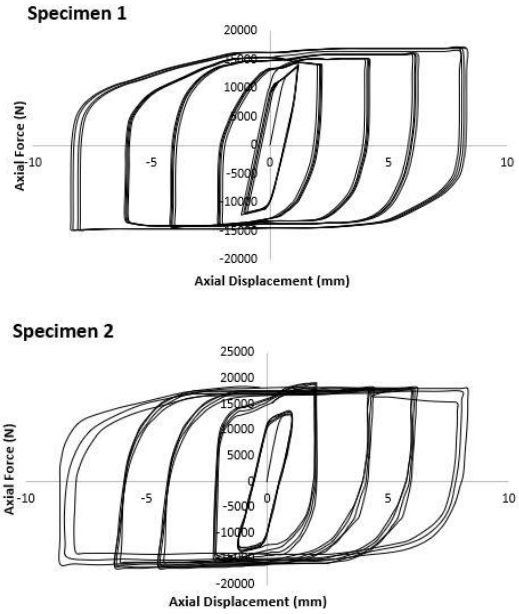

Fig. 7 Hysteretic response of the specimens tested

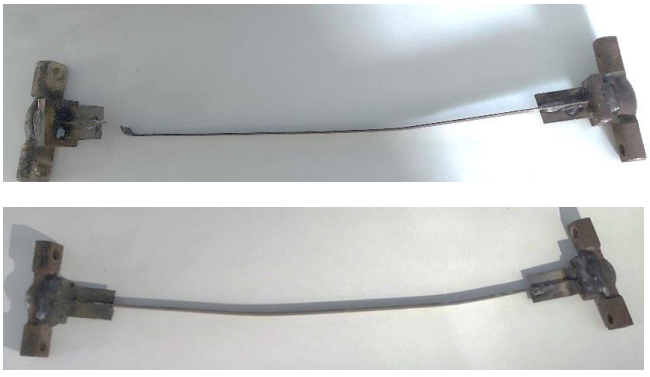

Fig. 8 Failure pattern of core part for specimen 1 (above) and specimen 2 (below)

4. Finite element modelling and validation

Over the past few decades, extensive numerical research and investigations have been conducted to assess the effectiveness and performance of BRBs. Researchers have employed 3D finite element analyses to study BRBs with various

configurations and material properties. Fahenstock et al. [14] conducted nonlinear dynamic analyses on BRB frames using scaled ground motion records at different seismic hazard levels. Takeuchi et al. [21] performed nonlinear analyses to understand the local buckling mechanism of the outer tube. Their findings indicated that larger gaps between the core and the outer tube, along with thinner tube thickness, resulted in a significant increase in tube strain rate. The length of the core member was found to have no effect on the brace's performance.

Korzekwa and Tremblay [22] conducted nonlinear analyses involving cyclic loading on all-steel BRBs, analyzing the nature of contact forces between the core member and the outer tube. They observed that these forces were resisted by tension in bolts and flexure in the tube. As a result, longitudinal frictional forces developed, leading to the generation of compressive loads acting axially in the outer tube during displacement cycles imposed on the brace. Dusicka and Tinker [23] investigated ultra-lightweight BRBs consisting of aluminium cores and bundled glass fibre-reinforced polymer pultruded tubes as restrainers. These BRBs were effective in resisting global buckling stability and weighed significantly less (27% of conventional filler-type BRBs and 41% of all-steel BRBs).

Further studies have also been conducted on all-steel BRBs. Anniello et al. [24] theoretically investigated the performance of dismountable all-steel BRBs through finite element analysis with the aim of upgrading existing RC buildings. Hoveidae and Rafezy [25, 26] performed finite element analyses on all-steel BRBs to study their overall and local buckling behavior. Karimi et al. [27] conducted finite element analysis on a three-story steel frame incorporating BRBs, investigating the seismic response of the frame under impact load and conducting dynamic analysis. Rossi [28] numerically examined BRBs using the isotropic hardening rule. Hosseinzadeh and Mohebi [29] compared the performance of all-steel BRBs with ordinary braces through finite element models and cyclic analysis. Almeida et al. [30] presented a case study on retrofitting an existing reinforced concrete school building with all-steel BRBs, demonstrating the effectiveness of BRBs in strengthening existing structures.

In addition, researchers have explored the integration of BRBs as energy dissipating devices in damped-outrigger systems [31]. Rahnavard et al. [32] proposed a method for accurately modelling and constructing a simple BRB model using finite element modelling with ABAQUS software. Avci-Karatas et al. [33] developed finite element models of BRB specimens based on full-scale experimental data [34], identifying key factors influencing the hysteretic behavior of BRBs. Alborzi et al. [35] proposed a hybrid BRB composed of multiple plates with different stress-strain behavior and compared its performance with conventional BRBs using time-history analysis. Jamkhaneh et al. [36] introduced a new type of all-steel BRB with corrugated edges, investigating its behavior through finite element modeling. They found that the corrugated and ribbed edges enhanced the buckling resistance of the braces. Naghavi et al. [37] numerically studied different types of concentrically braced frames and BRB frames using non-linear pushover analysis and time-history analysis.

In this study, 20 finite element analyses are conducted and studied on 12 all-steel BRB specimens with different restraining mechanisms, gaps, loading protocols, and core portions to study the effect of these parameters on the hysteretic behavior and energy dissipating capacity of all-steel BRBs.

4.1. Validation of finite element model

4.1.1. From literature available

With the aim of investigating the numerical behavior of the proposed BRB models, ABAQUS 6.13 software is used for non-linear finite element (FE) analysis. Beforehand, a BRB model based on past experimental research by Tabatabaei et al. (2014) is validated for its experimental and numerical results by performing finite element analysis on it. The loading protocol applied to the BRB model is as per Tabatabaei et al. [38]. Two cycles each for $\pm\Delta_{by}$, 0.5 $\pm\Delta_{bm}$, $\pm\Delta_{bm}$, 1.5 $\pm\Delta_{bm}$, and 2 $\pm\Delta_{bm}$ are applied as shown in Fig. 10. Here, Δ_{by} is the brace yield displacement, which is 1.7 mm, and Δ_{bm} is the axial displacement of the brace for the designed story drift, which is 27.7 mm. The material and geometric properties assigned to the model are the same as described in the literature [38]. The core is considered to be 80 mm in width and 10 mm in thickness, with a yield and ultimate strength of 235 MPa and 365 MPa, respectively. The end portions of the core are stiffened with two trapezoidal plates of 200 mm length, 80 mm width, and 10 mm thickness. The yield length of the core part is taken to be 1100 mm. The core is encased between two steel plates of 180 mm width and 10 mm thickness made from the same steel material as the core. The encasing plates are reinforced with square structural steel sections of 60 mm size and 5 mm thickness for out-of-plane action. The encasing plates are bolted with a filler plate along the length of the core. The core is further welded at both ends with square endplates of 300 mm size and 30 mm thickness. The modelling properties are also similar, with some minor changes. The identical parts were modelled and assembled as shown in Fig. 9, but somewhat finer meshing is used so as to obtain accurate results. 5 mm meshing is taken for all the parts,

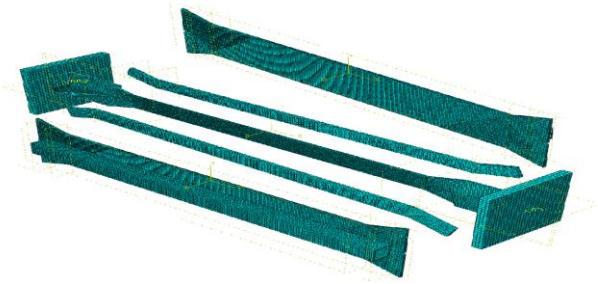

Fig. 9 Meshed parts of the model

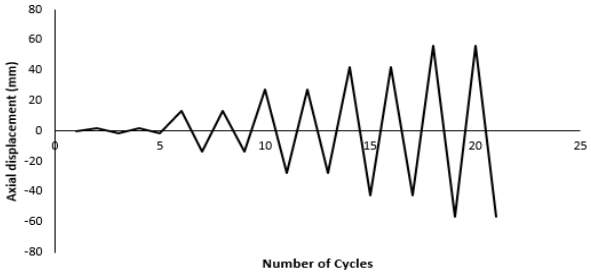

Fig. 10 Loading Protocol

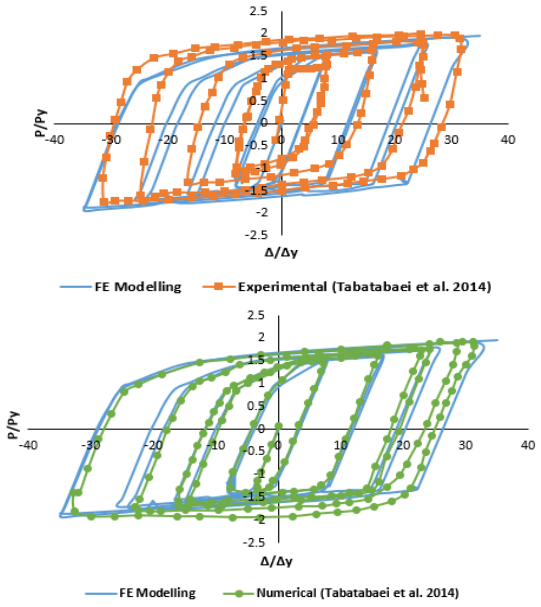

Fig. 11 Hysteretic curves obtained by FE modelling compared with experimental and numerical curves

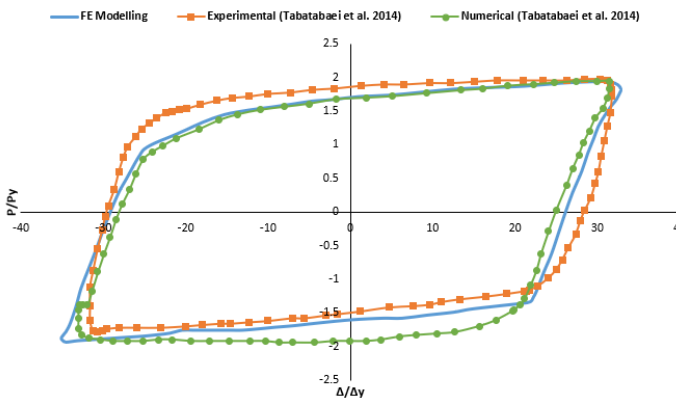

Fig. 12 Validation of hysteretic loop from FE modelling with experimental and numerical

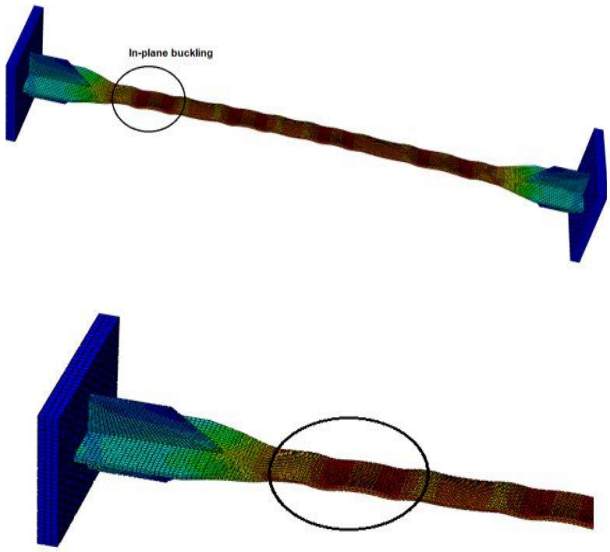

Fig. 13 Failure pattern observed

including the core, restraining plates with square hollow structural steel sections, filler plates, and endplates. A damping factor of 2E-4 is also introduced in the cyclic step to avoid the convergence problem. The hysteretic curve obtained with FE simulation is compared with that of the experimental and numerical one as shown in Figs. 11 and 12. A good correlation is observed between them. The failure pattern observed is also identical to the experimental result, as shown in Fig. 13. In-plane buckling and local buckling are observed along the yield length of the modelled BRB.

4.1.2. From experimental results

The specimens tested are also numerically investigated with ABAQUS 6.13 software. Both specimens are assigned their respective geometric and material properties as described in Section 2.1. The specimens are modelled using eight-node solid (C3D8R) elements with a reduced-integration technique and with 3D linear solid elements having three translational degrees of freedom per node. Nonlinear material modelling is done for core plates in both models and both elastic and plastic properties are assigned. A non-linear combined isometric and kinematic hardening rule with cyclic hardening is assigned for core parts in each model. The restrainer parts are assigned an elastic property only and are considered to remain elastic during the analysis. A friction coefficient of 0.1 is provided between the steel core plate surface and the angle restrainer surface to simulate the PTFE sheet in between. Finer meshing is done on the core parts of both models than on their respective restrainer parts (Fig. 14).

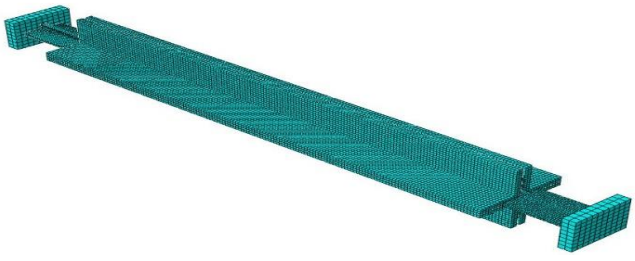

Fig. 14 Meshed FE models of specimen 1

The parts are prepared and assembled in the assembly by providing the required contact interaction. The combined hardening parameters assigned, including cyclic hardening, are material yield stress at zero plastic strain = 250 MPa, kinematic hardening parameter C = 10 GPa, Gamma1 = 48, rate factor b =4 and Q_∞ = 45 MPa [22]. An initial imperfection of L/400 is given to both models before the cyclic step, where L is the yielding length of the core.

The hysteretic curves obtained for specimen 1 are plotted with their FE results for each displacement level, as shown in Fig. 15. Each displacement level consists of four cycles of different frequencies. It can be seen that the hysteretic curves obtained for the specimen for experimental and numerical analysis are nearly identical for every displacement level. The hysteretic response of specimen 2 for all 5 displacement levels is also validated for its FE response (Fig. 16). The failure pattern obtained is also similar. Fig. 17 compares the failure pattern of specimen 2 for its experimental and FE results. Furthermore, the energy dissipated by the specimens at each level is calculated from the hysteretic loop obtained from the experimental and FE results and compared. Table 2 gives the energy dissipation comparison for both specimens.

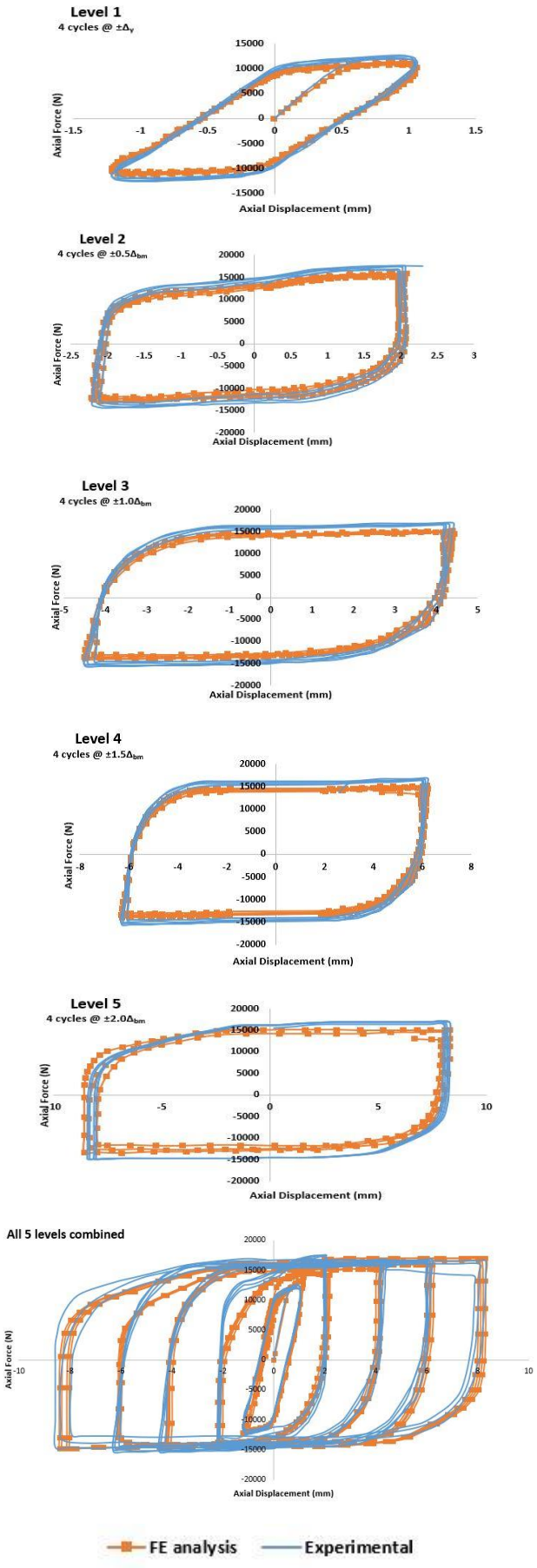

Fig. 15 Validation of experimental and FE results for specimen 1

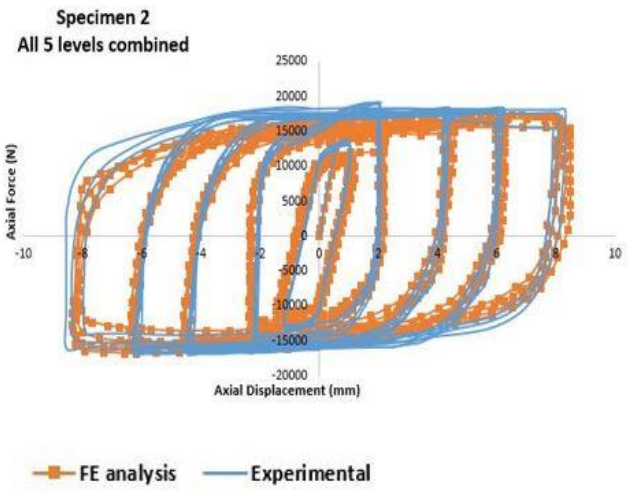

Fig. 16 Validation of experimental and FE results for specimen 2

Table 2
Energy dissipation by tested specimens

Specimen	Displacement Level	Energy dissipated (kN-mm)		Percentage difference (%)
		Experiment	FE analysis	
1.	1.	21.8	20.75	5.1
	2.	90.5	87.5	3.5
	3.	207.6	200	3.8
	4.	310	298	4.2
	5.	498	475	4.8
2.	1.	25.6	24.9	2.7
	2.	108.6	105	3.4
	3.	247.7	240	3.2
	4.	361.5	342.7	5.5
	5.	578	546.25	5.8

Fig. 17 Failure pattern observed in specimen 2 (experimental and FE)

4.2. Description of modelled parts

The finite element analysis for all the specimens was achieved with the help of the FE software ABAQUS 6.13. All the specimens are all-steel and have different parts that are assembled and then simulated. The specimens are grouped into two series depending on the restrainer used for the encasement of the core member, namely: (a) Series I and (b) Series II. The specimens with angle sections as restrainers are grouped in Series I, while the specimens with channel sections as restrainers are grouped in Series II. Both series are further subdivided into specimens, with the core having a stiffened transition portion and a non-stiffened transition portion. Table 1 gives a brief description of the specimens. The model name of the BRB specimens is in the form of codes ABRBij and CBRBij where, the indexes i and j represent the number of the model and type of specimen, whether stiffened or unstiffened, with letters S and U, respectively. ABRB stands for BRBs with angle sections used as restrainers, and CBRB stands for BRBs with channel sections used as restrainers. The different parts are assigned different material properties that are discussed in the next section.

4.3. Geometric and material properties

The geometric properties assigned to the specimens are briefly described in Table 3. A total of 20 finite element analyses are performed on 12 specimens that are divided into two series. All the specimens have the same core size of 40 mm x 8 mm. Series I includes six specimens, each having four angle sections with two filler plates as restrainer. Further, the size of the angle restrainer is different for every specimen. Each BRB is further divided into two types: the one with a stiffened transition portion and the other with an unstiffened one. Similarly, Series II has BRBs with two channel sections and two filler plates as restrainer, with each BRB having different sizes of channel sections for each specimen. The specimens are also subdivided on the basis of the stiffening of the transition portion. The filler plates are provided along the length of the core plates to prevent strong axis buckling. Further, a gap of 2 mm is provided between the filler plates and the core plate for Series I BRBs, and a gap of 1 mm is provided for Series II BRBs. A friction coefficient of 0.1 is provided between the restrainer and the core member so as to act as an unbonding agent. Fig. 18 explains the typical model of the proposed BRB specimens for both series.

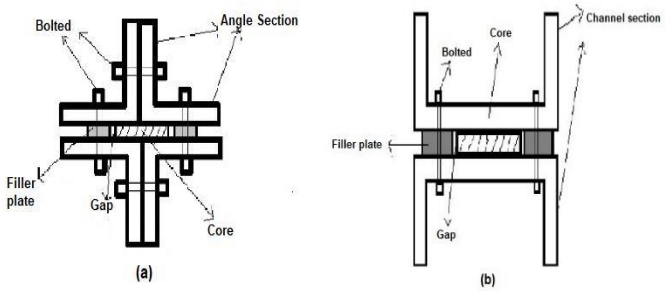

Fig. 18 Typical cross-section of proposed (a) Series I BRBs and (b) Series II BRBs

Table 3
Geometric properties of specimens

Series	Model name	Core dimensions (mm)	Restrainer dimensions (mm)	Area of core (mm^2)	Gap (mm)
I	$ABRB_{1S}$	40 x 8	4 ISA (50x50x3) + 2 filler plates	320	2
	$ABRB_{1U}$	40 x 8	4 ISA (50x50x3) + 2 filler plates	320	2
	$ABRB_{2S}$	40 x 8	4 ISA (55x55x5) + 2 filler plates	320	2
	$ABRB_{2U}$	40 x 8	4 ISA (55x55x5) + 2 filler plates	320	2
	$ABRB_{3S}$	40 x 8	4 ISA (60x60x5) + 2 filler plates	320	2
	$ABRB_{3U}$	40 x 8	4 ISA (60x60x5) + 2 filler plates	320	2
II	$CBRB_{4S}$	40 x 8	2 ISMC 100 + 2 filler plates	320	1
	$CBRB_{4U}$	40 x 8	2 ISMC 100 + 2 filler plates	320	1
	$CBRB_{5S}$	40 x 8	2 ISMC 125 + 2 filler plates	320	1
	$CBRB_{5U}$	40 x 8	2 ISMC 125 + 2 filler plates	320	1
	$CBRB_{6S}$	40 x 8	2 ISMC 150 + 2 filler plates	320	1
	$CBRB_{6U}$	40 x 8	2 ISMC 150 + 2 filler plates	320	1

The core plate is assigned the material properties of structural steel with a yield strength of 250 MPa. The core plate is also assigned plastic properties in addition to the elastic ones. The filler plates are simple structural steel plates. The restrainer angle sections and channel sections are assigned their respective properties on the steel table. The material properties assigned to core and filler plates are given in Table 4.

Table 4
Material properties of specimens

Parts	Density (kg/m^3)	Elastic Modulus (GPa)	Poisson's Ratio	Yield Strength (MPa)
Core	7780	210	0.3	250
Filler Plates	7760	210	0.3	-

4.4. Combined hardening parameters

A combined isotropic and kinematic hardening rule with cyclic hardening is used to analyze all the proposed models. Certain parameters need to be defined for such analyses in ABAQUS. These parameters include the kinematic hardening modulus *C*, the kinematic hardening rate parameter γ, the isotropic hardening magnitude for cyclic hardening Q_∞, and the isotropic hardening rate parameter *b* for cyclic hardening. Fig. 19 depicts the stress-plastic strain curve for steel and explains the variation of parameters *C* and γ for kth backstress.

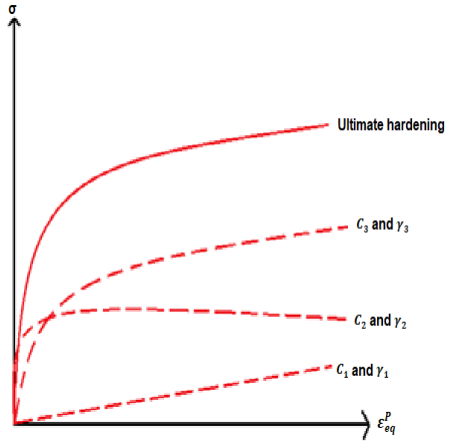

Fig. 19 Stress-plastic strain curve of steel

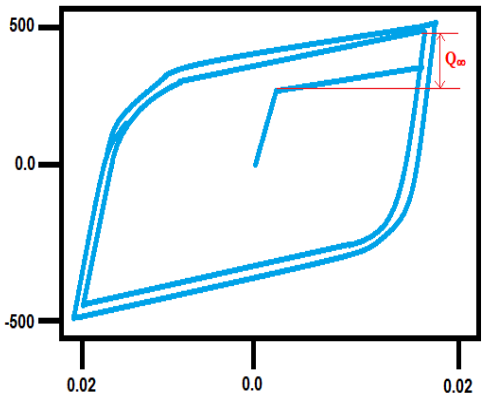

Fig. 20 True stress-strain curve for a metal

The uniaxial kinematic hardening modulus for the material can be given as [39]

$$H_u^{'} = \sum_k \left(C_k e^{-\gamma_k \varepsilon^P_{eq}} \right) \tag{7}$$

Here, C_k is the kinematic hardening modulus and γ_k is the kinematic hardening rate parameter for k^{th} backstress, respectively. The stress of the material for which the stress-strain curve is presented in Fig. 19 can be given as

$$\sigma = \frac{C}{\gamma}\left(1 - e^{-\gamma \varepsilon^P_{eq}}\right) \tag{8}$$

Here, γ is the rate at which *C* decreases with increasing equivalent plastic strain ε^P_{eq} [39]. The yield stress of the material can be given by

$$\sigma_y = \sigma_{y0} + Q_\infty \left(1 - e^{-b\varepsilon^P_{eq}}\right) \tag{9}$$

Where, σ_{y0} is the initial yield stress. Here, Q_∞ represents the maximum change in yield surface size in the true stress-strain plot (Fig. 20) and *b* defines the rate at which Q_∞ changes with increasing equivalent plastic strain.

These parameters are the material properties and can be found in the stress-strain curve of the core material. However, approximate values of such parameters are suggested by some researchers [40, 22]. Hartloper et al. [39] have proposed these parameters for structural steel in their research. For FE modelling purposes, these parameters can be assumed depending on the material selected and the values suggested in past research.

4.5. Modelling assumptions

Finite element models of all 12 specimens are developed using ABAQUS 6.13 software. All the specimens are modelled using eight-node solid (C3D8R) elements with a reduced-integration technique. The models are made in parts and then assembled to perform cyclic analysis. Every part is modelled using 3D linear solid elements with three translational degrees of freedom per node. Non-linear material modelling is done for the core plates in each model and is assigned both elastic and plastic properties. A non-linear combined isometric and kinematic hardening rule with cyclic hardening is assigned for core parts in each model. However, the restrainer parts are assigned an elastic property only and are considered to remain elastic during the analysis. The core part and the filler part are provided with a gap of 1 to 2 mm. The interaction property between the angle or channel section parts and the core parts is assigned a surface-to-surface contact property with tangential behavior. The frictional coefficient should be assumed carefully as the increase in the value of this coefficient increases the amount of axial force transmitted to the restrainer part. This further results in an increase in bending moment in the restrainer due to the P-Δ effect, and consequently, the global buckling load of the entire ASBRB may change. Hence, a friction coefficient of 0.1 is provided between the steel core plate surface and the restrainer surface to simulate a greasy, smooth surface between the core and the restrainer. The assumption of the friction coefficient is as per Chou et al. [41]. However, to simulate a rough and dry surface between the restrainer and the core element, the value of the frictional coefficient may be adopted as 0.3 [22].

Normal behavior as hard contact is also assigned between the core and the restrainer with nonlinear properties. The filler plate and the angle or channel restrainers are assumed to be connected with bolted connections along the length, and hence, to simulate this, the restrainer parts are connected to each other using a tie constraint. The full Newton-Raphson method was employed to solve the non-linear analysis. A fine mesh is employed for both the core plate and restrainer parts. For core plates with stiffened transition segments, partitioning of the plate is done to achieve a uniform and desired mesh. (Fig. 21).

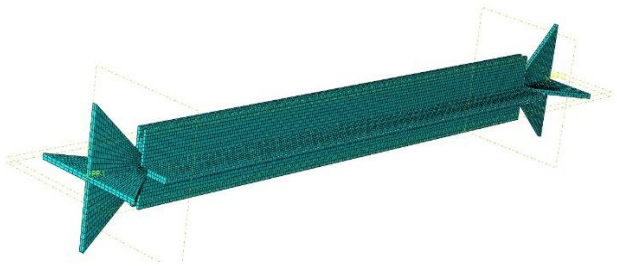

Fig. 21 Finite element model of $ABRB_{1S}$

The parameters used for a combined isometric and kinematic rule with cyclic hardening are material yield stress at zero plastic strain = 250 MPa, kinematic hardening parameter *C* = 10 GPa, Gamma1 = 48, rate factor *b* =4 and Q_∞ = 45 MPa [22]. An initial imperfection with a linear perturbation is also assigned as the initial step before the cyclic step. The initial geometric imperfection can be assigned in three ways: imperfection based on eigenmode data; imperfection based on static analysis data; and by directly defining the imperfection. In this analysis, an initial imperfection of 1 mm is assigned based on the first mode of buckling pattern. The first five buckling modes for the core plate with a stiffened transition portion can be seen in Fig. 23. An automatic stabilization with a damping coefficient of 1E-4 is applied to avoid convergence problems.

4.6. Loading protocols

Two different types of loading protocols are considered in this analysis. All 12 specimens are analyzed for the Type I loading protocol, which is shown in Fig. 20. In this loading protocol specimens are cyclically loaded at 8 different axial displacement levels, which are $1/3\Delta_y$; $2/3\Delta_y$; $1.0\Delta_y$; 0.33 Δ_{bm} (0.33%), $0.5\Delta_{bm}$ (0.5%), $1.0\Delta_{bm}$ (1%), $1.5\Delta_{bm}$ (1.5%), and $2\Delta_{bm}$ (2%). Two cycles of loading were applied at each displacement level, where Δ_y is the displacement that corresponds to the yielding of the core and Δ_{bm} is the axial deformation of the brace corresponding to the design story drift. In this study, Δ_{bm} was set to 10 mm, which corresponds to the axial strain of 1% in the core, and the core yielding displacement, Δ_y, was calculated as 1.27 mm based on the material characteristics. Hence, the ultimate axial displacement demand of the brace during cyclic loading was determined as $2\Delta_{bm}$=20 mm, which corresponds to a core strain of 2%. A similar loading pattern was considered by Eryasar [42] in his research. Eight specimens ($ABRB_{1S}$, $ABRB_{1U}$, $CBRB_{4S}$, $CBRB_{4U}$, $ABRB_{2S}$, $ABRB_{3S}$, $CBRB_{5S}$, and $CBRB_{6S}$) are also analyzed for the Type II loading protocol, which consists of two cycles at each deformation of an axial strain of 0.5, 1, 1.5, 2, 2.5, 3, and 3.5% with an increment of 0.5% after every two cycles. This type of loading pattern was considered by Sahoo and Ghowsi [43] in their experimental research. (Fig. 22).

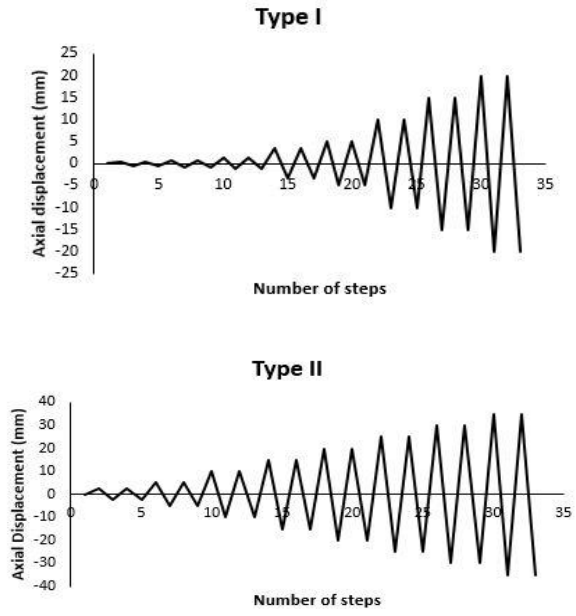

Fig. 22 Loading Protocols

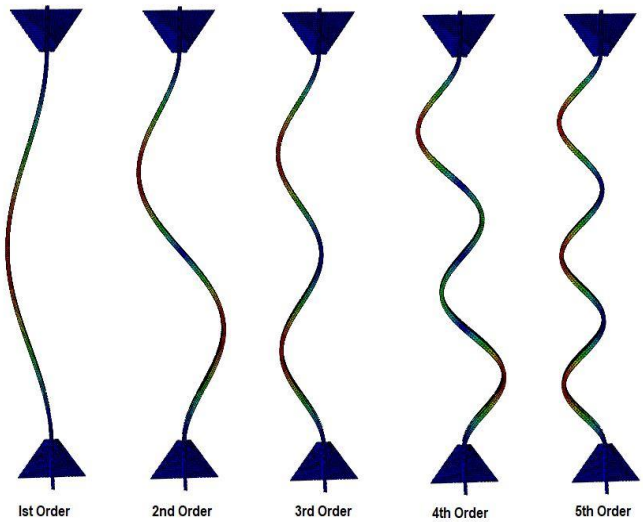

Fig. 23 First five buckling modes for core plate with stiffened transition portion

5. Results

5.1. Hysteretic loops

The hysteretic response of all 12 specimens for 20 different analyses is presented in Figs. 25 and 26. Normalized values for force and displacement are found for each specimen for plotting the curves to give a better understanding and comparison of the specimens. The compressive adjustment factor (β) and strain adjustment factor (ω) for all the specimens are calculated using equations (10) and (11) respectively.

$$\beta = \frac{C_{max}}{T_{max}} \tag{10}$$

$$\omega = \frac{T_{max}}{F_C A_C} \tag{11}$$

Where, F_c is the yield stress of the core plate, and A_c is the cross-section area of the core plate. β and ω values for all the modelled specimens are given in Tables 5 and 6 for both the loading types. It can be observed that these values are greatest for $ABRB_{4S}$ and are satisfactory for all other specimens. The β and ω values depend upon the type of contact and gap between the core and the restrainer member. β values are greater for direct contact because of high frictional forces generated at the core and the restrainer interface. The use of unbonding material or a gap between the core and the restrainer is therefore strongly recommended. All the specimen models in this study are thus provided with some gap between the core and the restrainer. β and βω values can also be found from the backbone curve of the ASBRB specimens, as shown for specimens $CBRB_{4S}$ and $ABRB_{3S}$ in Fig. 24. The strain adjustment values are needed for calculating the adjusted ASBRB strengths for design purposes. The energy dissipated by all the specimens is also calculated from their hysteretic responses for both loading types, as given in Table 7.

Table 5
Comparison of strength adjustment parameters for loading protocol Type I

Specimen	T_{max} (kN)	C_{max} (kN)	β	ω	βω
$ABRB_{1S}$	87	87	1.00	1.09	1.09
$ABRB_{1U}$	85	86	1.01	1.06	1.07
$ABRB_{2S}$	87	87	1.00	1.09	1.09
$ABRB_{2U}$	85	86	1.01	1.06	1.07
$ABRB_{3S}$	87	88	1.01	1.10	1.11
$ABRB_{3U}$	85	86	1.01	1.06	1.07
$CBRB_{4S}$	87	87	1.00	1.09	1.09
$CBRB_{4U}$	85	86	1.01	1.06	1.07
$CBRB_{5S}$	87	87	1.00	1.09	1.09
$CBRB_{5U}$	85	86	1.01	1.06	1.07
$CBRB_{6S}$	88	96	1.09	1.10	1.20
$CBRB_{6U}$	82	87	1.06	1.02	1.09

Table 6
Comparison of strength adjustment parameters for loading protocol Type II

Specimen	T_{max} (kN)	C_{max} (kN)	β	ω	βω
$ABRB_{1S}$	121	140	1.15	1.51	1.74
$ABRB_{1U}$	87	88	1.01	1.09	1.10
$ABRB_{2S}$	104	106	1.02	1.30	1.33
$ABRB_{3S}$	104	108	1.04	1.30	1.35
$CBRB_{4S}$	104	105	1.00	1.30	1.30
$CBRB_{4U}$	87	88	1.01	1.09	1.10
$CBRB_{5S}$	100	102	1.02	1.25	1.28
$CBRB_{6S}$	103	105	1.01	1.29	1.30

Table 7

Energy dissipated by the specimens

Specimen	Energy dissipated (kN-mm)	
	Type I	Type II
$ABRB_{1S}$	580	1300
$ABRB_{1U}$	440	950
$ABRB_{2S}$	520	1400
$ABRB_{2U}$	420	-
$ABRB_{3S}$	540	1400
$ABRB_{3U}$	460	-
$CBRB_{4S}$	520	1500
$CBRB_{4U}$	460	900
$CBRB_{5S}$	520	1400
$CBRB_{5U}$	440	-
$CBRB_{6S}$	900	1500
$CBRB_{6U}$	420	-

5.1.1. Type I loading

Specimens $ABRB_{1S}$ and $ABRB_{1U}$

It was observed from the hysteretic loops obtained from both these specimens that the specimen with an unstiffened transition portion, $ABRB_{1U}$ gives satisfactory performance up to 2% strain loading, and the energy dissipated is not much less than that by the specimen with a stiffened transition part, $ABRB_{1S}$. However, the specimen with a stiffened transition portion dissipates more energy and shows a better hysteretic response. The β and ω values for the former and latter are found to be 1.01 and 1.06; and 1.00 and 1.09, respectively.

Specimens $ABRB_{2S}$ and $ABRB_{2U}$

Both specimens whether with a stiffened transition core portion or without, show satisfactory hysteretic behavior and dissipate a comparable amount of energy, with a difference of 19%. The hysteretic curve obtained for specimen $ABRB_{2S}$, which dissipated a greater amount of energy, is somewhat better with more loops, which means stress distribution is more uniform. The β and ω values for both specimens are found to be 1.00 and 1.09; and 1.01 and 1.06, respectively, similar to the specimens discussed in the previous section.

Specimens $ABRB_{3S}$ and $ABRB_{3U}$

Specimen $ABRB_{3U}$ dissipated 0.85 times the energy dissipated by $ABRB_{3S}$, and both showed symmetrical hysteretic behavior. The β and ω values for both are found to be 1.01 and 1.10; and 1.01 and 1.06, respectively. No global buckling is observed, with some minor local buckling in both specimens.

Specimens $CBRB_{4S}$ and $CBRB_{4U}$

Stable hysteretic curves are obtained for both the BRBs. The energy dissipation is higher for $CBRB_{4S}$ when compared with $CBRB_{4U}$ as expected but by only 11%. The hysteretic loops are also better for $CBRB_{4S}$. The β and ω values for both are found to be 1.00 and 1.09; and 1.01 and 1.06, respectively. There is no global buckling observed in both BRBs.

Specimens $CBRB_{5S}$ and $CBRB_{5U}$

Both specimens dissipated a decent amount of energy with stiffened one dissipating more. Stable and symmetrical hysteretic behavior is observed in both the BRBs. The β and ω values for both are found to be 1.00 and 1.09; and 1.01 and 1.06, respectively. No global buckling is observed; however, in-plane buckling is observed in the specimen $CBRB_{5U}$.

Specimens $CBRB_{6S}$ and $CBRB_{6U}$

Specimen $CBRB_{6S}$ dissipated a considerable amount of energy, showed stable hysteretic behavior up to 2% strain, and further dissipated energy at higher strain levels. The specimen showed higher energy dissipation than any other specimen. The hysteretic curve formed by the specimen is symmetrical with some degradation. Specimen $CBRB_{6U}$ showed stable hysteretic behavior and dissipated satisfactory energy, though quite less than that by the specimen with a stiffened transition core portion. The β and ω values for both are found to be 1.09 and 1.10; and 1.06 and 1.02, respectively.

5.1.2. Type II loading

Specimens $ABRB_{1S}$ and $ABRB_{1U}$

A large amount of energy is dissipated by specimen $ABRB_{1S}$ compared to specimen $ABRB_{1U}$. Local buckling is observed in the specimen after a 2.5% strain rate. The specimen showed quite satisfactory hysteretic behavior with the hysteretic curve having a number of loops. The curve obtained is quite symmetrical up to 2.5% strain, and then degradation is visible with further strain loading. Specimen $ABRB_{1U}$ experienced in-plane buckling after 2% of the strain rate and stopped dissipating further energy after 2.5% strain loading. However, it showed stable hysteretic behavior. The β and ω values for the former and latter are found to be 1.15 and 1.51; and 1.01 and 1.09, respectively.

Specimens $CBRB_{4S}$ and $CBRB_{4U}$

Specimen $CBRB_{4S}$ experiences local buckling along the yield length of the core. Global buckling is not seen, but markable stress is induced in the restrainer portion, which can be seen in Fig. 25 (b). The hysteretic loop obtained is symmetric, as expected. For $CBRB_{4U}$, the energy dissipation is less when compared with $CBRB_{4S}$. It was observed that $CBRB_{4S}$ dissipates quite a higher amount of energy than the specimen $CBRB_{4S}$, but experienced local buckling for Type II loading. The β and ω values for both are found to be 1.1 and 1.3; and 1.01 and 1.09, respectively.

Specimens $ABRB_{2S}$ and $ABRB_{3S}$

Quite stable and symmetrical hysteretic behavior is obtained for specimen $ABRB_{2S}$ up to 3.5% strain with some degradation at the compression side, but a considerable amount of energy is dissipated by the specimen. Local buckling is observed along the yielding core length. A perfect symmetrical hysteretic curve is obtained for the specimen $ABRB_{3S}$, during the entire loading. The energy dissipated is satisfactory and similar to that of the former specimen. In-plane buckling is observed along the core length in the specimen. The β and ω values for both are found to be 1.02 and 1.3; and 1.04 and 1.3, respectively.

Specimens $CBRB_{5S}$ and $CBRB_{6S}$

The hysteretic curve obtained for the specimen $CBRB_{5S}$ is uniform and symmetrical up to 3% strain, and then degradation is observed on further loading. Energy dissipation is, however, satisfactory with local buckling along the yielding length of the core. A stable and symmetrical hysteretic curve is obtained for specimen $CBRB_{6S}$, with a higher amount of energy dissipation than the former specimen. The β and ω values for both are found to be 1.0 and 1.25; and 1.01 and 1.29, respectively.

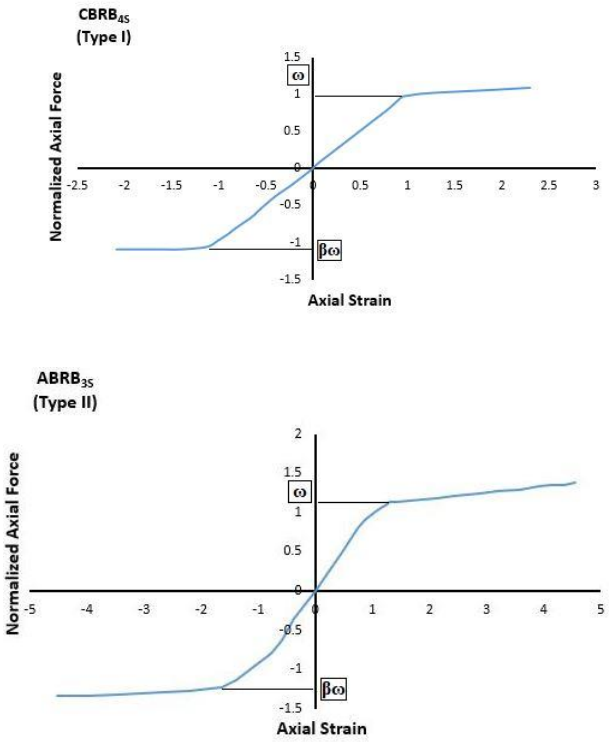

Fig. 24 Backbone curves for modelled ASBRBs

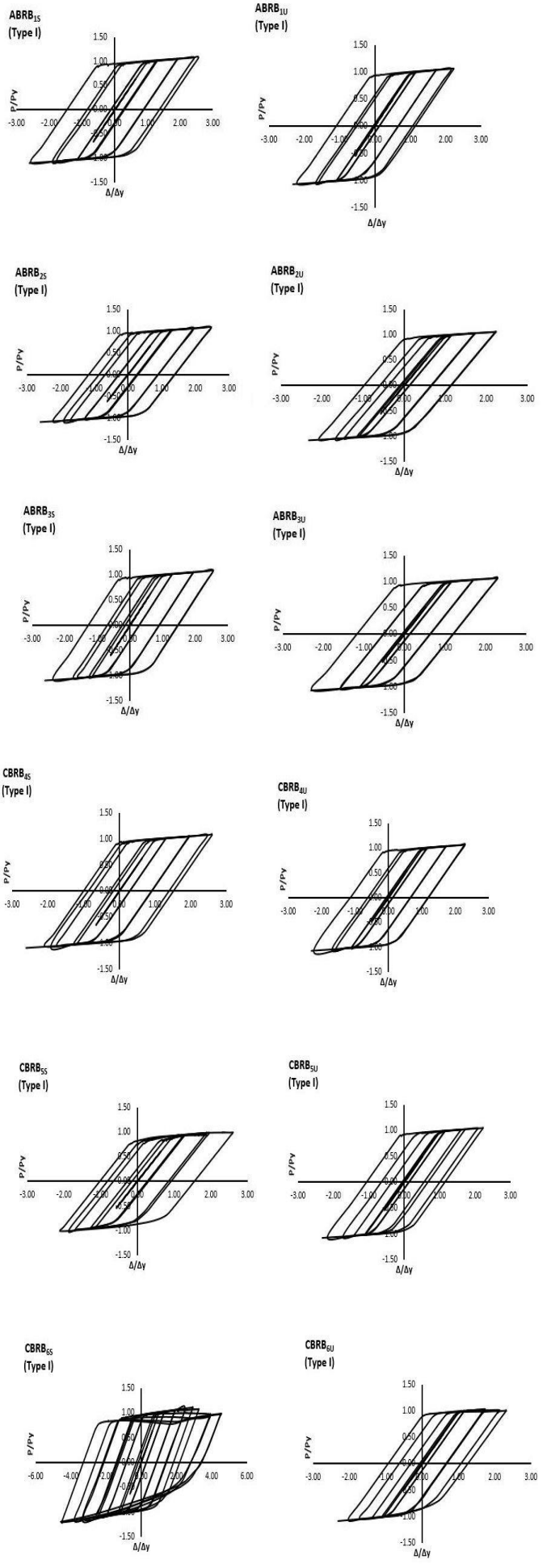

Fig. 25 Hysteretic responses for Type I loading protocol

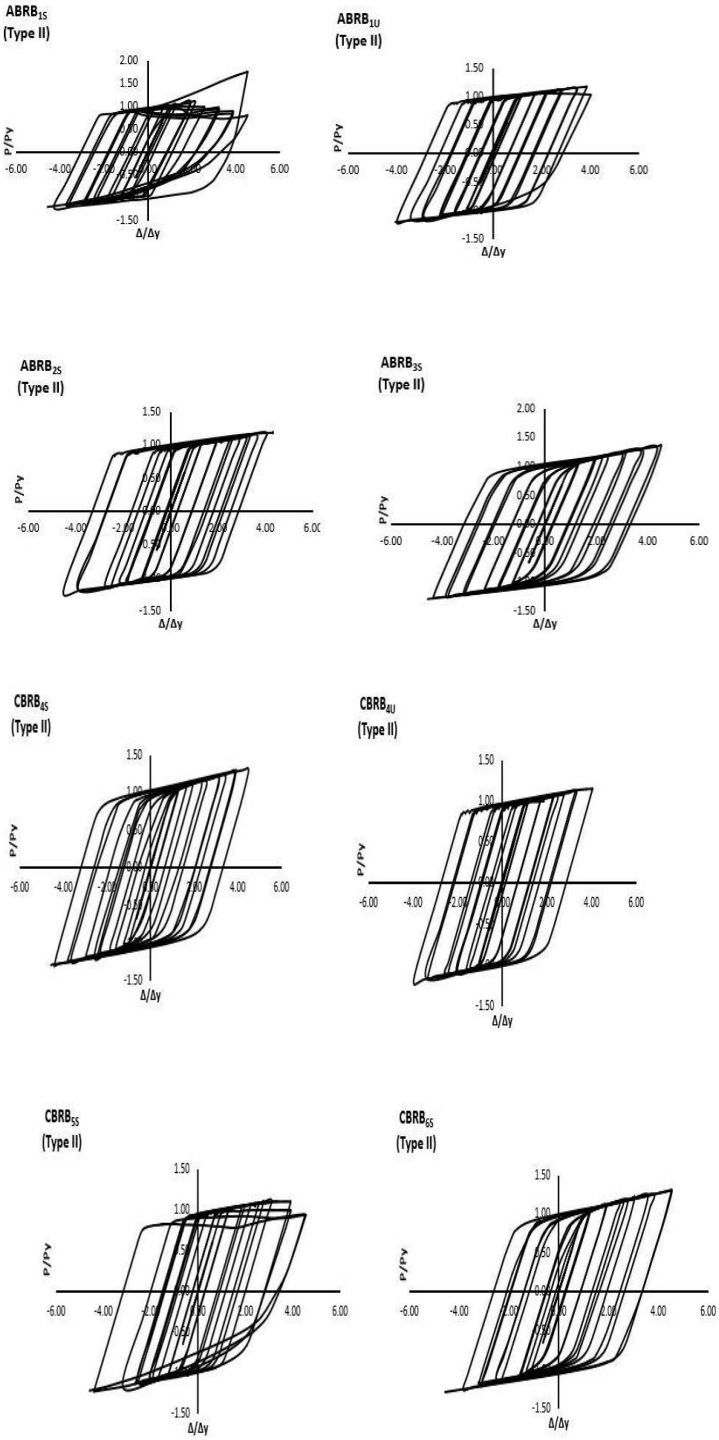

Fig. 26 Hysteretic responses for Type II loading protocol

5.2. Failure patterns

All the specimens showed a good hysteretic response and satisfactory energy dissipation for both types of loading patterns. For Type I loading, only in-plane buckling is observed in most of the specimens, with some minor local buckling along the core length. No global buckling is observed in any of the specimens for Type I loading. The specimens with unstiffened transition core portions performed well enough as compared with the specimens with stiffened transition core portions. However, for the Type II loading pattern, the specimens with stiffened transition portions performed much better. Local buckling is observed in almost all the specimens for Type II loading. Overall buckling is not seen in the specimens of this loading, but considerable stress is induced in the restrainers, which can be observed in some of the specimens. Fig. 27 shows the failure pattern and stress distribution pattern in the specimen $CBRB_{4S}$ for the Type II loading pattern.

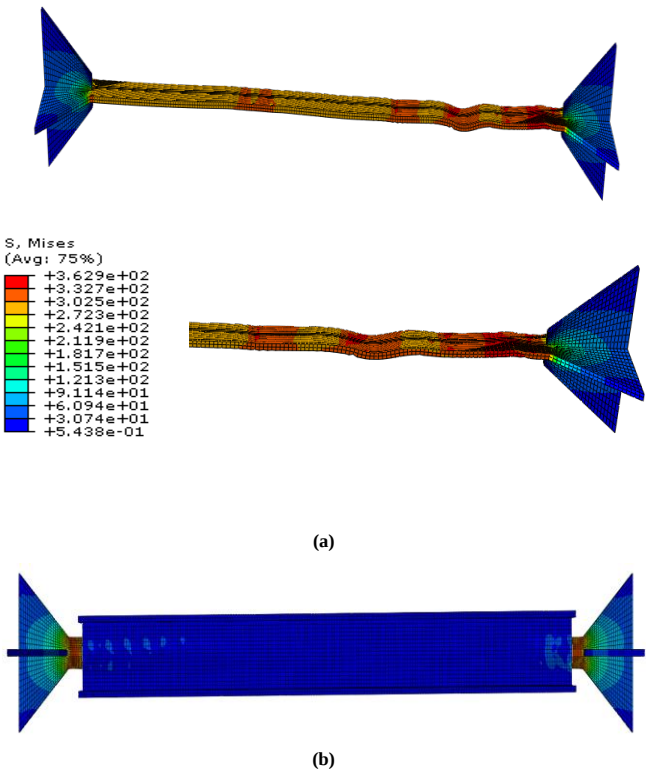

Fig. 27 Von-Mises Stress distribution in $CBRB_{4S}$ (a) core part and (b) entire BRB for Type II loading protocol

6. Conclusions

In a comprehensive study, a series of non-linear finite element analyses were conducted on 12 proposed All-Steel Buckling Restrained Brace (ASBRB) specimens. Prior to these analyses, two small-scale ASBRB specimens were subjected to cyclic testing to validate the experimental and finite element (FE) results. These specimens had different core cross-sections but utilized the same restraining arrangements, and they exhibited symmetrical hysteretic behavior. The dissipated energy of the tested specimens was compared between experimental and FE results. Additionally, the FE method used was validated by comparing the obtained results with literature from past research.

Subsequently, 20 non-linear FE analyses were performed on the proposed ASBRB specimens, considering various parameters. Based on these analyses, the following conclusions were drawn regarding the influence of these parameters:

Gap between Core and Restrainer: The size of the gap between the core and the restrainer was found to have a significant effect on the behavior of ASBRBs. Larger gaps resulted in increased energy dissipation capacity and improved overall performance.

Restrainer Material: The material used for the restrainer (steel or aluminium alloy) affected the behavior of ASBRBs. The choice of material influenced the stiffness and energy dissipation characteristics of the brace.

Core Stiffening: Stiffened and unstiffened types of core portions were investigated. It was observed that the inclusion of stiffening elements within the core enhanced the buckling resistance and energy dissipation capacity of ASBRBs.

Loading Protocols: Different loading protocols were examined to assess their impact on ASBRB behavior. The loading rate and sequence were found to influence the hysteretic response and energy dissipation characteristics of the braces.

By systematically varying these parameters and analyzing their effects, valuable insights were gained regarding the optimal configuration and design of ASBRBs. These findings contribute to the ongoing development and improvement of ASBRB technology, enhancing its effectiveness as an energy dissipating device in seismic-resistant structures.

6.1. Restraining mechanism

In the analyzed specimens, global buckling failure was not observed due to the strong restraining mechanism employed. The occurrence of global buckling failure depends on the ratio of the Euler buckling load of the restrainer to the yield load of the core part. If this ratio is greater than 1, the brace will not experience global buckling failure. All the specimens in the study had a ratio greater than 1, ensuring their resistance to global buckling.

However, it was found that the braces with channel restrainers outperformed the ones with angle restrainers in terms of energy dissipation. This suggests that the choice of restrainer design significantly influences the energy dissipation capacity of ASBRBs. It was also observed that local buckling occurred in the braces when the strain rate exceeded 2%.

To prevent global buckling, it is recommended to select restraining mechanisms with a value greater than 1.5, indicating that light sections can be chosen instead of heavy sections. Interestingly, the ASBRB with ISMC 150 as a restrainer, which is the heaviest restrainer among the proposed ASBRBs, achieved the maximum energy dissipation for both loading types.

These findings indicate that careful selection of the restrainer design, considering factors such as weight and the ratio of Euler buckling load to yield load, is crucial for optimizing the performance and energy dissipation capacity of ASBRBs.

6.2. Amount of gap

In the study, ASBRBs with angle restrainers had a 2 mm gap between the core member and the restrainer, while those with channel restrainers had a 1 mm gap. Surprisingly, the performance of the braces was found to be independent of the specific gap size (1 mm or 2 mm) in this study. The braces exhibited different behavior regardless of the gap size.

However, it is recommended to maintain a gap of 1 to 2 mm between the core member and the restrainer. This gap helps to prevent the transfer of axial load from the restrainer to the core and minimize the compression adjustment factor value. It is important to note that a larger gap can lead to undesirable consequences such as increased local buckling amplitudes and higher contact forces on the restrainer surface. These factors can ultimately result in a decrease in the strength of the ASBRB.

Therefore, while the specific gap size did not significantly affect the performance of the braces in this study, it is still necessary to maintain a suitable gap (1 to 2 mm) to ensure proper functioning and avoid potential issues related to strength and buckling.

6.3. Loading pattern

In this study, two different types of loading patterns were used: Type I loading, which followed the provisions prescribed by AISC (American Institute of Steel Construction), and Type II loading, which was based on the approach proposed by Sahoo et al. (2017). It was observed that ASBRB specimens could withstand higher strain rates than those prescribed in the AISC provisions.

The ASBRBs with stiffened transition portions exhibited good performance, particularly under higher strain rates. They were able to dissipate a significant amount of energy and exhibited a high number of symmetrical hysteretic loops during Type II loading.

The ratio of the yield load of the core part to the Euler buckling load of the restrainer (P_e/P_y) remained less than 1.5 for Type I loading. For Type II loading, this ratio increased for some ASBRBs but still remained below 2. It is worth noting that local buckling failure was observed in most cases during Type II loading, indicating the occurrence of localized buckling phenomena.

Overall, the study showed that ASBRBs have the capability to withstand higher strain rates and exhibit satisfactory performance, especially when equipped with stiffened transition portions. However, local buckling failures were observed in some cases during Type II loading.

6.4. Stiffening of the transition segment

Based on the simulations and findings of this research, ASBRBs without stiffened transition portions exhibited symmetrical hysteretic behavior for Type I loading. These braces performed satisfactorily and were able to dissipate energy up to a 2% strain rate. Although they dissipated less energy compared to ASBRBs with stiffened transition portions, they showed satisfactory performance, especially in buildings that are less prone to seismic attacks.

By not stiffening the transition portion of the core in ASBRBs used in such buildings, designers can achieve cost-cutting and material savings. It is recommended to use lightweight restrainers for ASBRBs, as they are replaceable and easy to handle. A gap of 1 to 2 mm between the core and the restrainer is sufficient to avoid transferring axial load and minimize compression adjustment factor values.

For structures with lower design story drift, ASBRBs with unstiffened transition portions in the core can be employed as cost-effective replaceable fuses. However, it is important to note that experimental validation of the finite element simulations conducted in this research is necessary. The authors plan to conduct such experimental validation in the future to further validate their findings.

Acknowledgment

The manuscript was developed at the Visvesvaraya National Institute of Technology (VNIT) in Nagpur, India. The authors acknowledge and express gratitude to VNIT for the support provided to the first author during her doctoral research. Additionally, the authors extend their thanks to the Motibagh Workshop of South East Central Railways (SECR) for their assistance in executing the experimental research conducted for the study.

Conflict of interest

There was no conflict of interest in the preparation of this manuscript.

References

[1] Yue Y. C., Bai Y. T., Wang Y., Ma X. F., Wang Y. H. and Li X. H., Experimental behavior and design of rectangular concrete filled tubular buckling-restrained brace, Advanced Steel Construction, 2021,Vol. 17 No. 4, pp. 366–375. DOI: 10.18057/IJASC.2021.17.4.5.

[2] Wakabayashi M., Nakamura T., Kashihara A., Yokoyama H., and Morizono T., Experimental study on the elasto-plastic behavior of braces enclosed by precast concrete panels under horizontal cyclic loading (Part 1 and Part 2) (1973), Summaries of Technical Papers of Annual Meeting of Architectural Institute of Japan Kinki Branch-Structural section I 1973; 6:121–8 (in Japanese).

[3] Kano Y., Kuwabara T., Seki Y. and Yoshino T., Experimental study on shear wall with braces (Part 1), Annual Research Meeting Architectural Institute of Japan, Kanto area, Japan, September; 1971. (in Japanese).

[4] Kimura K., Yoshioka K., Takeda T., Furuya N. and Takemoto Y., Tests on braces encased by mortar in-filled steel tubes, Annual Research Meeting Architectural Institute of Japan, Tokai area, Japan, October; 1976. (in Japanese).

[5] Mochizuki N., Murata Y., Ando N. and Takahashi S., Experimental study on buckling of unbonded braces under axial compressive force (Part 1 and Part 2), Annual Research Meeting Architectural Institute of Japan, Tokai area, Japan, September; 1979. (in Japanese).

[6] Mochizuki N., Murata Y., Ando N. and Takahashi S., Experimental study on buckling of unbonded braces under axial compressive force (Part 3), Annual Research Meeting Architectural Institute of Japan, Kinki area, Japan, September; 1980. (in Japanese).

[7] Fujimoto M., Wada A., Saeki E., Watanabe A. and Hitomi Y., A study on brace enclosed in buckling-restrained mortar and steel tubes (Part 2). Annual Research Meeting Architectural Institute of Japan, Kanto Area, Japan, October; 1988. (in Japanese).

[8] Fujimoto M., Wada A., Saeki E., Takeuchi T. and Watanabe A., Development of unbonded brace, 1990, Quarterly column no. 115, pp. 91-96.

[9] Takeuchi T., Wada A., Matsui R., Silter B., Lin P. C., Sutcu F., Sakata H. and Qu Z., Buckling-Restrained Braces and Applications, Japan Society of Seismic Isolation, 2017.

[10] Wada A., Connor J. J., Kawai H., Iwata M. and Watanabe A., Damage tolerant structures, Proceedings of first U.S.-Japan workshop on the improvement of building structural design and construction practices, September 8-10, 1992, San Diego, California.

[11] Black C. J., Makris N., and Aiken I. D., Component Testing, Stability Analysis, and Characterization of Buckling Restrained Braces, 2002, Univ. of California, Berkeley, CA.

[12] Sabelli R., Mahin S. and Chang C., Seismic demands on steel braced frame buildings with buckling-restrained braces, Eng. Struct., 2003, pp. 655–666.

[13] AISC 341-05. Seismic provisions for structural steel buildings. Chicago, IL, USA: American Institute of Steel Construction; 2002.

[14] Fahnestock L. A., Ricles J. M. and Sause R., Experimental evaluation of a large-scale buckling-restrained braced frame, J. Struct. Eng., 2007.

[15] AISC (American Institute of Steel Construction). Seismic provisions for structural steel buildings, Chicago, IL; 2010.

[16] Wu B., and Mei Y., Buckling mechanism of steel core of buckling-restrained braces, Journal of Constructional Steel Research, 2015, 107, pp. 61–69.

[17] Black C. J., Makris N., and Aiken I. D., Component Testing, Seismic Evaluation and Characterization of Buckling Restrained Braces, J. Struct. Eng., 2004, 130(6): pp. 880-894.

[18] Xie Q., State of the art of buckling-restrained braces in Asia, J. Constr. Steel Res., 2005, pp. 727–748.

[19] Wang C., Li T., Chen Q., Wu J., and Ge H., Experimental and Theoretical Studies on Plastic Torsional Buckling of Steel Buckling-restrained Braces, Advances in Structural Engineering, 2015, Vol. 17 No. 6, pp. 871-880.

[20] Yin Z. Z., Feng D. Z., Yang B. and Pan C. C., The seismic performance of double tube buckling restrained brace with cast steel connectors, Advanced Steel Construction, 2022, Vol. 18 No. 1, pp. 436–445. DOI: 10.18057/IJASC.2022.18.1.2.

[21] Takeuchi et al., Estimation of cumulative deformation capacity of buckling restrained braces. Journal of Structural Engineering, 2008, Vol. 134, No. 5, pp. 822– 31.

[22] Korzekwa A. and Tremblay R., Numerical simulation of the cyclic inelastic behavior of buckling restrained braces, In: 6th Int. Conf. on Behaviour of steel structures in seismic areas (STESSA 2009), Philadelphia, The Netherlands,

[23] Dusicka P. and Tinker J., Global Restraint in Ultra-Lightweight Buckling-Restrained Braces, J. Compos. Constr., 2013, 17(1), pp. 139-150.

[24] Aniello M., Corte G. D. and Landolfo R., Finite Element Modelling and Analysis of "All-Steel" Dismountable Buckling Restrained Braces, The Open Construction and Building Technology Journal, 2014, 8, (Suppl 1: M4), pp. 216-226.

[25] Hoveidae N. and Rafezy B., Overall buckling behavior of all-steel buckling restrained braces, J. Constr. Steel Res., 2012, pp. 151–158.

[26] Hoveidae N. and Rafezy B., Local Buckling Behaviour of Core Plate in All-Steel Buckling Restrained Braces, International Journal of Steel Structures, 2015, 15(2), pp. 249-260.

[27] Karimi M. R. B., Yaghin M. A. L., Nezhad R. M., Sadeghi V. and Aghabalaie M., Seismic Behavior of Steel Structure with Buckling-Restrained Braces, International Scholarly and Scientific Research & Innovation 9(4) 2015.

[28] Rossi P. P., Importance of Isotropic Hardening in the Modeling of Buckling Restrained Braces, J. Struct. Eng., 2015, 141(4): 04014124.

[29] Hosseinzadeh Sh. and Mohebi B., Seismic evaluation of all-steel buckling restrained braces using finite element analysis, Journal of Constructional Steel Research, 2016, 119, pp. 76–84.

[30] Almeida A., Ferreira R., Proenca J. M. and Gago A. S., Seismic retrofit of RC building structures with Buckling Restrained Braces, Engineering Structures, 2017, 130, pp. 14–22.

[31] Lin P. C., Takeuchi T. and Matsui R., Seismic performance evaluation of single damped-outrigger system incorporating buckling-restrained braces, Earthquake Engng Struct Dyn., 2018, 47, pp. 2343–2365.

[32] Rahnavard R., Naghavi M., Aboudi M. and Suleiman M., Investigating modeling approaches of buckling-restrained braces under cyclic loads, Case Studies in Construction Materials, 2018, 8, pp. 476–488.

[33] Avci-Karatas C., Celik O. C. and Eruslu S. O., Modeling of Buckling Restrained Braces (BRBs) using Full-Scale Experimental Data, KSCE Journal of Civil Engineering, 2019, 23(10), pp. 4431-4444.

[34] Avci-Karatas C., Celik O. C., and Yalcin C., Experimental investigation of aluminum alloy and steel core buckling restrained braces (BRBs), Int. J. Steel Struct., 2018, Vol. 18, No. 2, pp. 650-673.

[35] Alborzi M., Tahghighi H. and Azarbakht A., Numerical comparison on the efficiency of conventional and hybrid buckling-restrained braces for seismic protection of short-to-mid-rise steel buildings, International Journal of Advanced Structural Engineering, 2019, 11, pp.439–454.

[36] Jamkhaneh M. E., Ebrahimi A. H. and Amiri M. S., Investigation of the Seismic Behavior of Brace Frames with New Corrugated All-Steel Buckling Restrained Brace, International Journal of Steel Structures, 2019, https://doi.org/10.1007/s13296-018-00202-2.

[37] Naghavi M., Rahnavard R., Thomas R. J. and Malekinejad M., Numerical evaluation of the hysteretic behavior of concentrically braced frames and buckling restrained brace frame systems, Journal of Building Engineering, 2019, 22, pp. 415–428.

[38] Tabatabaei S. A. R., Mirghaderi S. R. and Hosseini A., Experimental and numerical developing of reduced length buckling-restrained braces, Engineering Structures, 2014, (77), pp. 143–160.

[39] Hartloper A. R., Sousa A. C. and Lignos D. G., Constitutive Modeling of Structural Steels: Nonlinear Isotropic/Kinematic Hardening Material Model and Its Calibration, J. Struct. Eng., 2021, 147(4): 04021031. DOI: 10.1061/(ASCE)ST.1943-541X.0002964.

[40] Tremblay R., Bolduc P., Neville R. and DeVall R., Seismic testing and performance of buckling restrained bracing systems. Can J Civ Eng 2006;33(1): pp. 183-98.

[41] Chou C. and Chen S., Sub-assemblage tests and finite element analyses of sandwiched buckling restrained braces. Eng Struct 2010;32:2108-21.

[42] Eryasar M., Experimental and numerical investigation of buckling restrained braces, A thesis submitted to the graduate school of natural and applied sciences of middle east technical university, 2009.

[43] Sahoo D. R. and Ghowsi A. F., Experimental Study of All-Steel Buckling-restrained Braces under Cyclic Loading, International conference on earthquake engineering and structural dynamics, 12-14 June 2017, Reykjavik, Iceland.

[44] Lopez W. A. and Sabelli R., Seismic Design of Buckling-Restrained Braced Frames, Structural steel education council, 2004.